AGU PUBLICATIONS

JGR

Journal of Geophysical Research: Atmospheres

RESEARCH ARTICLE
10.1002/2015JD024596

Key Points:
- High-accuracy balloon positions are retrieved from dual-frequency GPS receivers
- Improvements of balloon positions are assessed
- Impacts of the position improvements on the gravity wave parameter estimation are studied

Supporting Information:
- Supporting Information S1

Correspondence to:
W. Zhang,
zhangweixing89@whu.edu.cn

Citation:
Zhang, W., J. S. Haase, A. Hertzog, Y. Lou, and R. Vincent (2016), Improvement of stratospheric balloon GPS positioning and the impact on gravity wave parameter estimation for the Concordiasi campaign in Antarctica, *J. Geophys. Res. Atmos.*, *121*, 9977–9997, doi:10.1002/2015JD024596.

Received 2 DEC 2015
Accepted 12 AUG 2016
Accepted article online 15 AUG 2016
Published online 1 SEP 2016

©2016. American Geophysical Union. All Rights Reserved.

Improvement of stratospheric balloon GPS positioning and the impact on gravity wave parameter estimation for the Concordiasi campaign in Antarctica

Weixing Zhang[1,2,3], Jennifer S. Haase[2], Albert Hertzog[4], Yidong Lou[3], and Robert Vincent[5]

[1]School of Geodesy and Geomatics, Wuhan University, Wuhan, China, [2]Scripps Institution of Oceanography, University of California, San Diego, La Jolla, California, USA, [3]GNSS Research Center, Wuhan University, Wuhan, China, [4]Laboratoire de Météorologie Dynamique/IPSL, UPMC Univ Paris 06, CNRS, Palaiseau, France, [5]Physics Department, University of Adelaide, Adelaide, South Australia, Australia

Abstract Gravity waves (GWs) play an important role in transferring energy and momentum from the troposphere to the middle atmosphere. However, shorter-scale GWs are generally not explicitly resolved in general circulation models but need to be parameterized instead. Super pressure balloons provide direct access to measure GW characteristics as a function of wave intrinsic frequency that are needed for these parameterizations. The 30 s sampling rate of the GPS receivers carried on the balloons deployed in the 2010 Concordiasi campaign in the Antarctic is much higher compared to the previous campaigns and can cover the full range of the GW spectrum. Two among 19 balloons are also equipped with the dual-frequency GPS receivers initially developed for GPS radio occultation research in addition to the single-frequency receivers, which are expected to provide better positions for GW parameter estimations. Improvements of the positions are significant, from ~3–10 m horizontal and ~5 m vertical to ~0.1 and 0.2 m, respectively, which makes it possible to resolve the Eulerian pressure independently of altitude for the intrinsic phase speed estimation. The lower position accuracy in the previous analysis of campaign results from the single-frequency GPS receiver was primarily due to a problem with the onboard clock that is not present in the new results. The impacts of the position improvements on the final GW parameters are highlighted, with larger difference in momentum flux for the shorter-scale GWs than for the longer scale GWs and significant difference in the distribution of the intrinsic phase speed.

1. Introduction

Internal gravity waves (GWs) play a crucial role in transferring energy and momentum from the troposphere to the middle atmosphere [*Fritts and Alexander*, 2003]. The global pole-to-pole Brewer-Dobson circulation driven by planetary and gravity wave breaking in the stratosphere and mesosphere induces significant changes in temperature from radiative equilibrium [*Andrews et al*., 1987; *Hamilton*, 1995]. On a smaller scale, GWs also provide significant fluctuations of wind and temperature, which are linked to the formation of polar stratospheric clouds and related microphysical processes [*Dörnbrack et al*., 2002; *Höpfner et al*., 2006]. Owing to their spatial scales, gravity waves are generally too short to be explicitly resolved by general circulation models (GCMs) so their effects have to be parameterized [*Kim et al*., 2003]. However, results will differ with different gravity wave drag parameterization schemes [*Charron et al*., 2002]. An important difficulty in the development of these parameterizations is the poor understanding of the intensity of wave sources, in particular, the global distribution of momentum flux [*Fritts and Alexander*, 2003]. A variety of techniques have greatly improved our knowledge of gravity wave characteristics. For example, gravity wave momentum flux has been measured with ground-based radars [*Vincent and Reid*, 1983], radiosondes [*Allen and Vincent*, 1995], satellite instruments such as the Cryogenic Infrared Spectrometers and Telescopes for the Atmosphere (CRISTA) [*Eckermann and Preusse*, 1999; *Ern et al*., 2004] and the High Resolution Dynamics Limb Sounder (HIRDLS) [*Alexander et al*., 2008], and GPS radio occultation observations [*Tsuda et al*., 2000; *Baumgaertner and McDonald*, 2007]. Nevertheless, these observations still suffer from poor geographic coverage, short duration, or limited spatial resolution. Importantly, frequencies are always measured in a ground-based reference frame rather than in the frame moving with the background wind. It is the latter frequency, the intrinsic frequency, which determines wave properties.

Superpressure balloons (SPBs), which float on isopycnic or constant density surfaces, have been used in both troposphere and lower stratosphere studies since the early 1960s [*Julian et al*., 1977]. The balloons drift with the horizontal wind as quasi-Lagrangian tracers in the atmosphere, providing a direct way to measure the properties of GWs as a function of wave intrinsic frequency. Compared to ground- or space-based observations, SPB has the advantages of both fully characterizing wave packets and providing information over wide geographic regions during long duration flights [*Alexander et al*., 2010]. In particular, SPBs are the best platform for measuring the intermittency of GW flux with profound consequences for GW forcing of mean flow. For example, for the same long-term mean momentum flux, intermittent GWs with higher amplitude will break lower in the atmosphere than those produced by a steady source [*Hertzog et al*., 2008].

The Concordiasi field campaign launched a constellation of 19 balloons developed by the Centre National d'Etudes Spatiales (CNES, the French space agency) from McMurdo station (77°51′S, 116°40′E) in 2010 [*Rabier et al*., 2010]. A similar campaign in 2005, the Vorcore campaign, was very successful and provided significant knowledge on the characteristics of gravity waves in the Antarctic region [*Vincent et al*., 2007; *Boccara et al*., 2008; *Hertzog et al*., 2008, 2012]. However, an important limitation of the Vorcore observations was the relative low sampling period (15 min) of the Global Positioning System (GPS) receivers due to the low data transmission capability. The corresponding Nyquist period (30 min) is much longer than the Brunt-Väisälä period (approximately 5 min in the lower stratosphere in the Antarctic region), the cutoff period of gravity waves. In the subsequent Concordiasi campaign, the improved data transmission system enabled the GPS receivers to record observations at 30 s intervals, which means full coverage of the GW spectrum. The better GPS vertical position accuracy (~1.5 m) improves by nearly 10 times over that achieved in the Vorcore campaign, making it possible to use a more direct and accurate method to estimate the GW parameters [*Vincent and Hertzog*, 2014]. Furthermore, two of the 19 balloons in the Concordiasi campaign carried high-accuracy, dual-frequency GPS receivers developed originally for GPS radio occultation (ROC). These data make it possible to attempt much higher precision GPS positioning based on the PPPAR (Precise Point Positioning with Ambiguity Resolution) [*Zumberge et al*., 1997; *Ge et al*., 2008] technique, with an expected improvement in GW parameter retrievals.

The paper is organized as follows: The data and strategy used in the balloon position estimation based on the PPPAR method are described in the second section and the positioning precision is evaluated and compared to the standalone GPS receiver used in previous studies in the third section. In the fourth section, a spectral analysis of the balloon position time series over the Antarctic Peninsula is presented. The fifth section describes the method used in the wavelet analysis for GW parameter estimation. The improvement of the GW parameter estimation due to the higher precision positions is described. Discussion and conclusions follow in section 6.

2. Data and Strategy

2.1. Concordiasi Campaign

The Concordiasi campaign, a joint French-United States initiative, took place over the Antarctic region in 2010. It aimed to reduce uncertainties in atmospheric models in the Southern Hemisphere, providing validation data for satellite sounding, and for studying gravity waves [*Rabier et al*., 2010]. Nineteen helium-filled superpressure balloons with 12 m diameter were launched between September 2010 and January 2011. The scientific payload common to all balloons included a single-frequency GPS receiver to measure the balloon positions with a 30 s sampling rate and instruments to measure air temperature and pressure. The balloon positions were calculated onboard in real time and sent back to the ground.

Balloon 18 (referred as PSC18—for Physics and Stratospheric Chemistry) was also equipped with a GPS radio occultation equipment package, including two high-accuracy and dual-frequency GPS receivers sampling at 30 s [*Haase et al*., 2012]. PSC18 was launched on 29 September 2010 and flew for 54 days. One receiver recorded continuously over the entire campaign, and the second receiver recorded data on only one day, 13 October 2010, in order to evaluate balloon dynamics. Because of data transmission bandwidth limitations, the sample rate for both receivers was shifted to 60 s for the time period when two receivers were operating. PSC19 carried one such receiver, sampling at 30 s for the whole period. It was released on 8 October 2010 and flew for 42 days. Instead of recording receiver positions directly, the GPS carrier phase and pseudorange observations were recorded by the onboard receivers and sent back to the ground for precise positioning analysis.

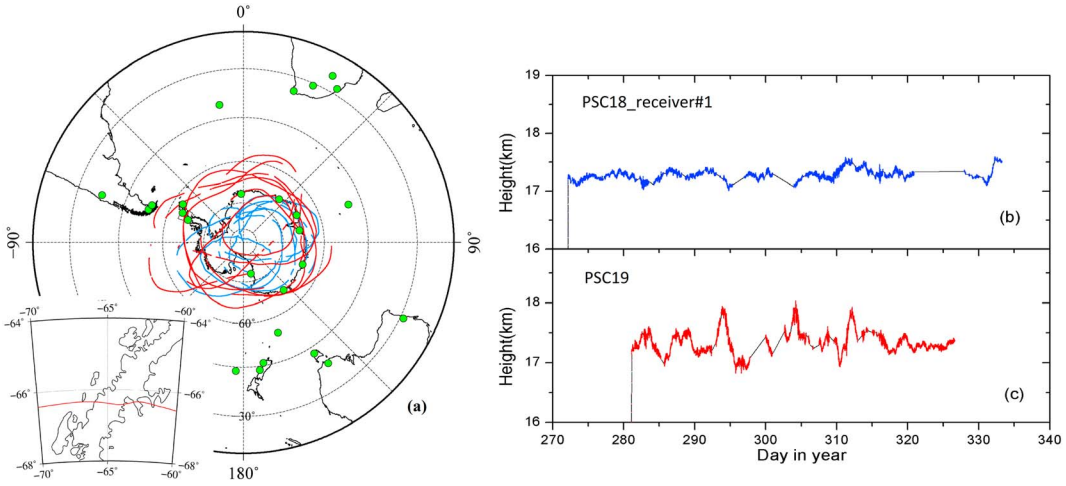


Figure 1. Ground-based GPS station distribution and balloon trajectories: (a) Green dots denote the ground-based GPS stations from the IGS network used for satellite clock and FCB estimation. The blue line and red line are the trajectories of GPS receiver #1 on PSC18 and the receiver on PSC19, respectively. The Antarctic Peninsula region is enlarged in the inset figure when PSC19 passes over the Antarctic Peninsula on 7 November 2010; (b) Altitude time series derived from the ROC GPS receiver #1 on PSC18 and (c) from the ROC GPS receiver on PSC19. Data gaps are indicated by straight lines.

2.2. Precise Point Positioning With Ambiguity Resolution

Compared to the ~1–2 m balloon position accuracy derived in real time from single-frequency receiver, as assumed in *Vincent and Hertzog* [2014] (referred to as VH14 hereafter), the high-accuracy dual-frequency receivers carried on PSC18 and PSC19 have the potential to get much higher position accuracy. This has a direct impact on GW parameter retrievals. Analyzing the data after transmission to the ground allows use of precise orbital information and the use of advanced methods to remove other positioning errors such as ionospheric and neutral atmospheric effects, satellite and receiver clock errors, and the resolution of the integer number of cycle ambiguities in the interferometric carrier phase measurements. Because of the relatively sparse distribution of ground-based GPS reference stations in the Antarctic region and the dynamics of the balloons, the PPPAR method is used to estimate the 3-D positions of the balloons. Twenty-eight GPS ground stations distributed in Antarctica and the surrounding southern continents from International Global Navigation Satellite Systems (GNSS) Service (IGS) network (Figure 1) are selected to estimate the regional satellite clock errors and the carrier wave fractional cycle bias (FCB) products. The estimated regional satellite clock products are used instead of the global satellite clock products (for example, the IGS final clock product) in PPPAR since the estimated regional clock errors can compensate for some other unmodeled errors [*Lou et al.*, 2014]. The FCB products are utilized for the ambiguity resolution for higher accuracy in PPPAR [*Ge et al.*, 2008; *Geng et al.*, 2010] compared to the conventional PPP (Precise Point Positioning) method [*Zumberge et al.*, 1997].

The GPS final orbit products provided by IGS and the known differential code biases between frequencies from the Center for Orbit Determination in Europe (CODE) are used. Antenna phase center corrections [*Schmid et al.*, 2007], phase wind-up corrections [*Wu et al.*, 1993], and relativity corrections are applied. In the first step satellite clock errors are estimated as parameters with white noise variance and then are held fixed in the FCB solution in the next step and in the final step of the PPPAR positioning calculation. Wide-lane FCB is taken as constant over a day, while narrow-lane FCB is estimated every 15 min as described in *Ge et al.* [2008]. Ground-based GPS station positions from IGS SINEX (Solution INdependent EXchange format) products are fixed in the satellite clock error and FCB estimation. Receiver positions on the balloon are estimated in kinematic mode without any constraints between consecutive epochs. Ionospheric delays are eliminated by using the ionosphere-free combination of phase and pseudorange observations. Neutral atmospheric zenith total delays are constrained with an a priori Saastamoinen model [*Saastamoinen*, 1972] based on pressure and temperature taken from global pressure and temperature model [*Boehm et al.*, 2007]. Corrections to the zenith wet delay (ZWD) component at the ground stations are estimated as a random walk process with a power density of 20 mm/$\sqrt{\text{h}}$ in the satellite clock error and FCB estimation

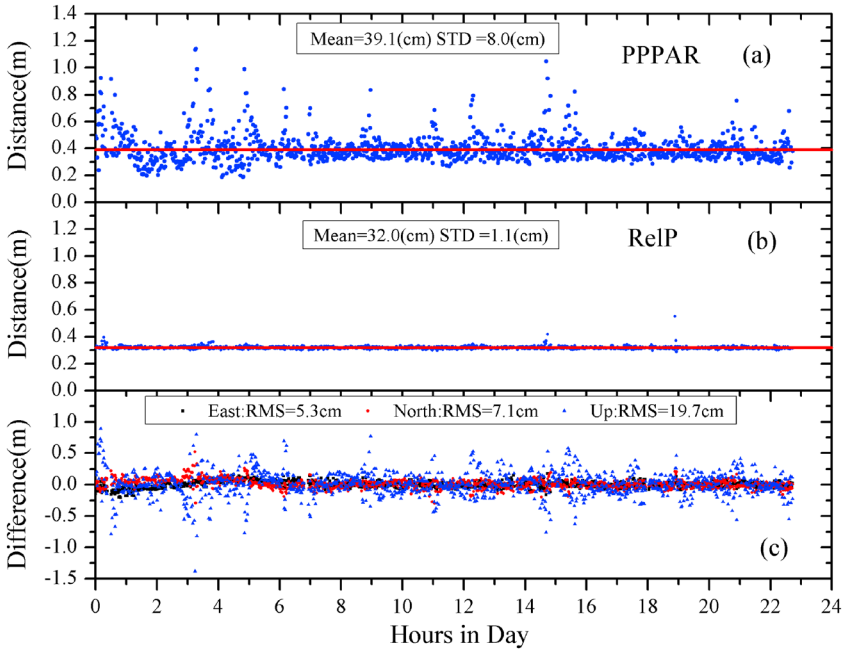


Figure 2. Comparison of PPPAR and RelP solutions: (a) Time series of the baseline distance between the two receivers on PSC18 derived from the PPPAR solutions. The mean value and standard deviation are given at the top of the panel and the mean value is also indicated with the red horizontal line; (b) similar to Figure 2a but derived from RelP solutions; (c) Differences of the baseline from PPPAR and RelP solutions in the east (black), north (red), and vertical (blue) components. The RMS values of the differences are also indicated at the top of the panel.

steps. For a balloon at ~17–18 km in the Antarctic region the ZWD parameters are very small and can be neglected in the PPPAR step. Neglecting the ZWD correction significantly reduces the number of estimated parameters and improves the solution stability. In all calculations, receiver clock errors are estimated at each epoch as parameters with white variance. All satellite clock error estimation, FCB estimation, and PPPAR are based on the PANDA (Position And Navigation Data Analyst) [*Shi et al.*, 2008] package developed at Wuhan University.

3. Positioning Assessment

It is not possible to evaluate the balloon position accuracy independently due to the absence of the known true value of the positions. Fortunately, we have two receivers with constant separation on PSC18 and they recorded GPS data simultaneously on 13 October 2010 (day of year (DOY) 286). This makes it possible to assess the PPPAR-based position accuracy by comparing with the baseline solutions based on a relative positioning (RelP) method. The baseline was processed using GrafNav GNSS postprocessing software developed by NovAtel in a kinematic mode. Time series of the derived distance between the two antennas on PSC18 are shown in Figure 2b. In the RelP method, almost all of the errors described in the correction method for the PPPAR absolute position are common to the two receivers so are negligible in the solution for the short distance between them. The standard deviation (STD) of the baseline distance time series is around 1.1 cm, which is sufficiently accurate to be taken as truth in assessing PPPAR accuracy. The distance calculated by the two receiver positions derived from the PPPAR solutions is shown in Figure 2a, with an STD of around 8 cm and a bias of about 7 cm from the known separation of 32 cm. The differences of the baseline in the east, north, and vertical component derived from PPPAR and RelP solutions are shown in Figure 2c. The horizontal positions differences are smaller, with root-mean-square (RMS) values of ~5.3 cm and 7.1 cm in the east and north components, respectively, compared with the vertical positions (RMS of ~19.7 cm). Therefore, the respective accuracies of the balloon positions derived from PPPAR solutions are around 3.5 cm, 5.0 cm and 14.0 cm in the east, north, and vertical components if we assume that the two receivers have the same accuracy (divide the RMS of differences by a factor of $\sqrt{2}$).

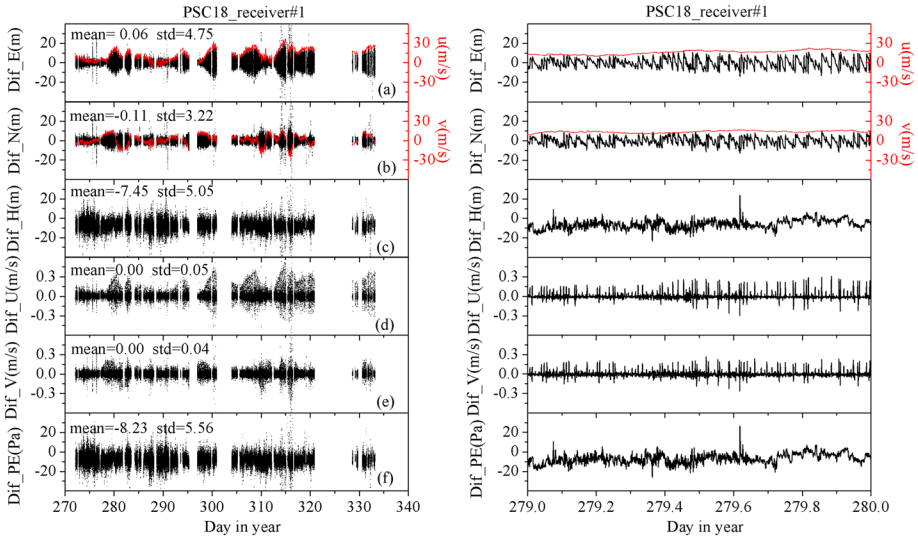


Figure 3. (left column) Differences between time series of the entire flight derived from PPPAR solutions and RTP solutions of PSC18 for: (a) position in east component, (b) position in north component, (c) altitude, (d) zonal velocity, (e) meridional velocity, and (f) Eulerian pressure perturbation. The mean value and the standard deviation of the time series are indicated in each panel and the zonal and meridional velocities are also plotted with red dots in Figures 3a and 3b. (right column) As for Figure 3 (left column) but only for 1 day. Spikes in velocity are clearly marked when the RTC clock is reset.

3.1. Position and Velocity Improvements

The single-frequency GPS receivers carried by all 19 balloons in the Concordiasi campaign calculate the 3-D positions on board in real time and, instead of GPS observations, transmit the positions every 30 s to the ground. All previously published gravity wave information are based on these single-frequency receiver measurements. However, the positions were not time stamped with the GPS time but by an onboard real-time clock (RTC) in order to ensure a time stamp for all of the data streams even when the GPS information was lost. Unfortunately, the RTC time is output with a precision of 1 s. During each flight, the onboard RTC time drifted and when the time difference between the RTC and the GPS time exceeded 1 s, the RTC was reset to the GPS time. The real-time positions recorded by the single-frequency receivers and the derived velocities (referred as RTP solutions) are compared with solutions derived from the high-accuracy GPS receivers based on the PPPAR method in order to evaluate the improvements by using the high-accuracy GPS receivers. The differences of positions and velocities for the entire flight periods are presented in Figures 3 and 4 for PSC18 and PSC19, respectively. The two high-accuracy receivers (receiver #2) on PSC18 operated simultaneously only for 1 day for the purpose of the estimating the rotation of the balloon and will not be used in the comparison here.

As can be seen in Figure 3, there is a strong correlation between the magnitude of the horizontal position differences and the horizontal velocity. This is because the position biases contributed by the clock stamp errors increase when the balloon moves faster, producing a position error that is proportional to velocity. Many jumps in the horizontal position differences can be seen in the zoomed 1 day time series. Those jumps occur at times when the RTC was reset, over intervals usually shorter than 30 min. The mean values of the position differences in the east and north components are 0.06 m and 0.11 m, respectively. The mean difference of about −7.45 m in the altitude is due to the fact that these two kinds of GPS receivers are placed in two separate gondolas with an offset of ~8 m beneath the balloon. The STD of position differences in the east, north, and vertical components is 4.75 m, 3.22 m and 5.05 m, which are significantly poorer than the assumed accuracies used in VH14 of 0.75 m in the horizontal and 1.5 m in the vertical positions. There are no obvious systematic biases in the horizontal velocities when averaged over the entire flight, with STD of 0.05 ms^{-1} and 0.04 ms^{-1} in the zonal and meridional velocity, respectively.

PSC19 was launched later than PSC18 and flew over a wider area with a faster velocity in the stratosphere, which resulted in larger positional differences than for PSC18. The position STD values are 9.61 m, 5.33 m, and 5.11 m in the east, north, and vertical components. The corresponding respective STDs for the zonal and meridional velocity components are 0.11 ms^{-1} and 0.10 ms^{-1}.

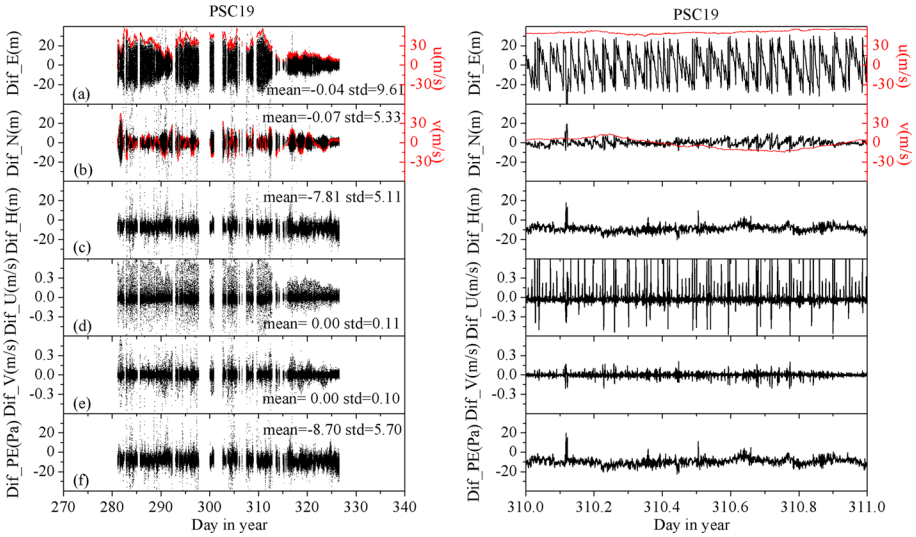


Figure 4. (left column) Differences between time series of the entire flight derived from PPPAR solutions and RTP solutions of PSC19 for: (a) position in east component, (b) position in north component, (c) altitude, (d) zonal, velocity, (e) meridional velocity, and (f) Eulerian pressure perturbation. The mean value and the standard deviation of the time series are indicated in each panel and the zonal and meridional velocities are also plotted with red dots in Figures 4a and 4b. (right column) As for Figure 4 (left column) but only for 1 day. Spikes in velocity are clearly marked when the RTC clock is reset.

The spikes in the velocity differences at the RTC reset epochs can reach several decimeters per second. We believe that the later momentum flux calculation will filter out spikes with frequency components higher than the buoyancy frequency (period ~5 min). For the zonal and meridional velocity differences, the STDs of the filtered time series are 0.04 ms^{-1} and 0.03 ms^{-1} for PSC18 and 0.07 ms^{-1} and 0.05 ms^{-1} for PSC19, respectively. These values are larger than velocity uncertainties assumed in VH14 (0.025 ms^{-1}).

4. Characteristics of Gravity Waves in the Balloon Position Time Series

4.1. Balloon Trajectory

The horizontal trajectories and the altitude time series of PSC18 and PSC19 derived from the PPPAR method are shown in Figure 1. Altitude has been converted from the World Geodetic System 1984 (WGS84) reference ellipsoid height, which is directly determined from GPS observations, to the orthometric height above sea level based on the Earth Gravitational Model 1996 (EGM96) [*Lemoine et al.*, 1998]. The difference between height above the reference ellipsoid and mean sea level, which is used in atmospheric measurements and models, varies from −106 to 85 m due to variations of mass distribution within the Earth, which cannot be neglected in these measurements.

As can be seen from Figure 1, the flight of PSC19, which was launched later than PSC18, covered a wider domain and the amplitude of the altitude fluctuation is larger than PSC18. There are some data gaps for both balloons due to data transmission constraints, making the time series discontinuous. Considering the significant contribution of the topography to the gravity wave generation, we focus on a 3 day continuous period from 6 November to 8 November 2010, including the event when PSC19 passed over the Antarctic Peninsula on 7 November. The trajectory of PSC19 when passing over the peninsula is also shown at the bottom left of Figure 1a where a significant deviation in the trajectory is visible. Studies have shown that the topography of the Antarctic Peninsula can induce strong gravity waves [*Bacmeister et al.*, 1990; *Wu and Jiang*, 2002; *Baumgaertner and McDonald*, 2007; *Plougonven et al.*, 2008]. The horizontal velocities deduced from positions through a finite differencing method, the altitude, the air temperature, and air pressure measured by PSC19 are presented in Figure 5. We assumed that the SPB is a perfect tracer of the horizontal wind in the atmosphere [*Vial et al.*, 2001]. All time series in Figure 5 exhibit strong fluctuations during the period indicated by two vertical black lines at the time when the balloon passed over the Antarctic Peninsula.

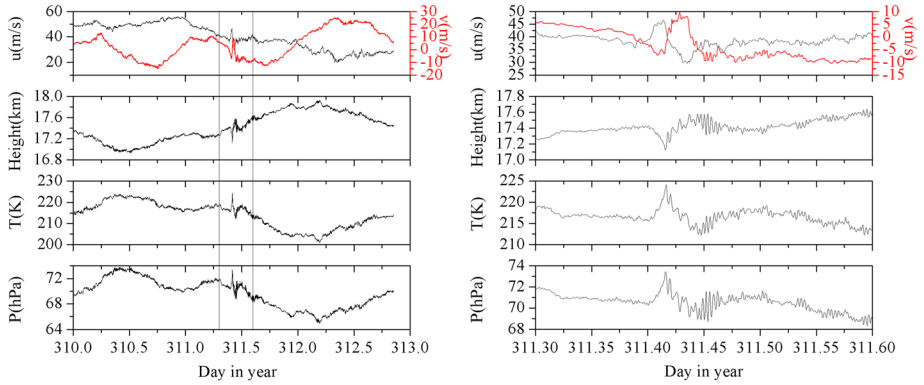


Figure 5. (left column) Time series for PSC19 from 6 November (DOY 310) to 8 November (DOY 312) 2010 and (right column) the zoomed time series during the period indicated by the two vertical black thin lines when the balloon passed over the Antarctic Peninsula. The time series from top to bottom show horizontal velocities, MSL (Mean Sea Level) altitude, air temperature, and air pressure (Lagrangian).

The polarization relations for pure gravity waves (i.e., $\hat{\omega} >> \hat{f}$ where $\hat{\omega}$ and $\hat{f}$ denote the intrinsic and inertial frequency in rad/s, respectively) can be expressed in a simplified form [*Fritts and Alexander*, 2003; *Plougonven et al*., 2008] as

$$\widetilde{u} = \frac{k}{l}\widetilde{v} \tag{1a}$$

$$\frac{\widetilde{T}}{\overline{T}} = -\frac{\hat{N}^2}{g}\widetilde{\zeta}. \tag{1b}$$

Here $\left(\widetilde{u}, \widetilde{v}, \widetilde{\zeta}, \widetilde{T}\right)$ are the complex amplitudes of the zonal velocity, meridional velocity, vertical air parcel displacement, and air temperature perturbations from the background; (k, l) are the zonal and meridional wave numbers; $\overline{T}$ is the background temperature; $\hat{N}$ denotes the Brunt-Väisälä frequency (buoyancy frequency) in rad/s, and g is the Earth gravitational constant. The eastward wind blowing over the mountain range of the Antarctic Peninsula, which has a southwest-northeast orientation, generates gravity waves with $k \sim -l < 0$. Therefore, according to equation (1a), there should be a 180° phase difference between the wave-induced zonal and meridional velocity perturbations. This is seen to first order in the time series in Figure 5, which are dominated by the large mountain waves with intrinsic period of ~1–2 h (significantly smaller than the average 13 h inertial period) during DOY 311.40 and 311.45. Similarly, the wave-induced altitude and temperature perturbations are roughly in antiphase, as expected according to equation (1b). However, it should be noted that an SPB does not undergo vertical displacements that are exactly the same as the parcel displacements because it floats on an isopycnic surface (see VH14).

4.2. Spectral Analysis

The quasi-Lagrangian superpressure balloons enable estimation of the intrinsic frequency spectrum. The power spectral density (PSD) of the zonal and meridional velocities from PSC19 from DOY 310 to DOY 312 are estimated based on the Welch method [*Welch*, 1967] using a Fourier transform with a window length of 2048 points (30 s interval), with a Hamming window taper and 50% overlap. The results are presented in Figure 6, where the average inertial period of ~13.1 h (2.1×10^{-5} Hz) at the balloon latitude and buoyancy period of ~300 s (3.3×10^{-3} Hz) are indicated by the red vertical dashed lines (f and N denote inertial and buoyancy frequency in Hz, respectively). A peak is visible near the buoyancy frequency for both spectra. For gravity waves in the range from the inertial frequency to buoyancy frequency, the horizontal wind velocity frequency spectra are expected to follow a negative power law [*Fritts and Alexander*, 2003] with typical exponent values in the range of 1 to 2, with most slopes falling close to five thirds when computed from ground-based measurements. The estimated slopes of the spectra for gravity waves observed in intrinsic frequency from the Lagrangian balloon platform shown in Figure 6 are 1.95 (zonal) and 1.97 (meridional). These results are consistent with the results of ~2 in *Hertzog and Vial* [2001] and *Hertzog et al*. [2002] in intrinsic frequency. Significant departures of the PSD from the power law spectra

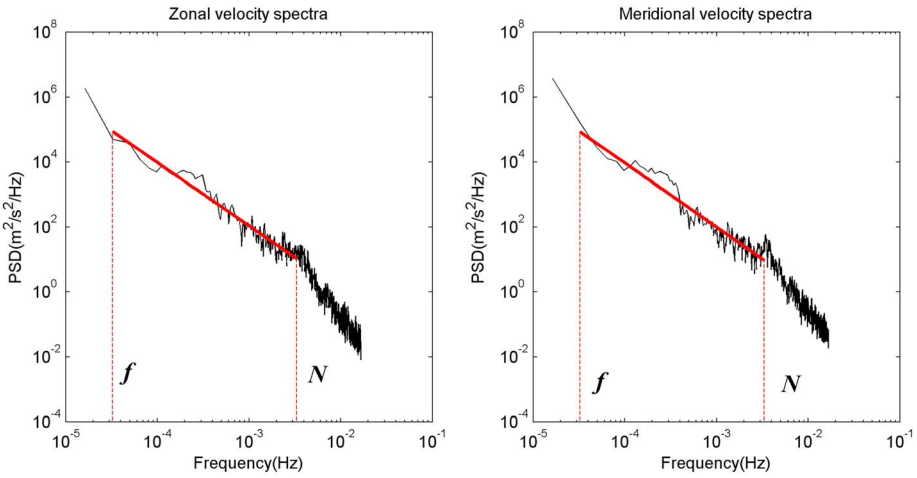


Figure 6. (left) Zonal and (right) meridional velocity spectra from flight PSC19 from DOY 310 to DOY 312. The red dash lines indicate the inertial (*f*) and buoyancy frequency (*N*) and the bold red lines are the fit to the total energy spectra based on a power law assumption.

can be found in the frequency range from 1×10^{-4} to 4×10^{-4} Hz, which corresponds to periods for the mountain waves induced by the topography in the Antarctic Peninsula.

5. Gravity Wave Parameter Retrieval and Comparison

5.1. Gravity Wave Parameter Retrieval

Observational studies have highlighted that gravity waves are generally observed as wave packets rather than as a spectral continuum [e.g., *Alexander and Pfister*, 1995; *Eckermann and Preusse*, 1999]. Instantaneous snapshots of high-resolution numerical simulations also tend to exhibit wave signatures that are associated with wave packets [*Watanabe et al*., 2008]. This packet-like description implicitly stresses that gravity wave activity in the atmosphere is intermittent [*Alexander et al*., 2010; *Hertzog et al*., 2012; *Wright et al*., 2013]. Several recent studies further describe observations of the intermittent nature of gravity waves [*Wright et al*., 2015; *Cao and Liu*, 2016; *John and Kumar*, 2016], which motivates us to use a wavelet analysis method to retrieve GW parameters.

The 3-D positions of the balloon and their errors impact the GW parameters in different ways. The momentum flux is directly dependent on the horizontal velocities derived from horizontal positions, and the intrinsic phase speed retrieval depends on the horizontal velocity and the vertical position used in the estimation of the Eulerian pressure perturbation. Gravity wave parameters, including momentum flux and intrinsic phase speed, are retrieved from the measurements following the procedures given in *Boccara et al*. [2008] (referred to as B08 hereafter). However, in that paper a hydrostatic assumption was made for the gravity waves in the retrievals because of the large uncertainties in the vertical positions. We use the method as given in VH14 instead, where altitude and pressure are explicitly resolved due to the much better GPS vertical precision in the Concordiasi campaign. We briefly introduce the retrieval algorithm here, while more details can be found in B08 and VH14.

The zonal and meridional velocities (u,v) of the balloon are first calculated from the horizontal positions by central finite differencing. The density (ρ) is estimated from the measured pressure (p_L, Lagrangian pressure) and temperature (T) through the ideal gas law. The GPS altitudes (ellipsoidal height) are converted to orthometric height (ζ_b) above sea level using EGM96. Excluding the launch period, the flight-mean values of $(\overline{u},\overline{v},\overline{p}_L,\overline{\zeta}_b)$ are calculated and removed from the time series to get the perturbation time series (u',v',p_L',ζ_b'). The Eulerian pressure perturbation (p_E') is then estimated from

$$p_E' = p_L' + \overline{\rho} g \zeta_b' \tag{2}$$

where p_L' is the Lagrangian pressure perturbation and $\overline{\rho}$ is the flight-mean density.

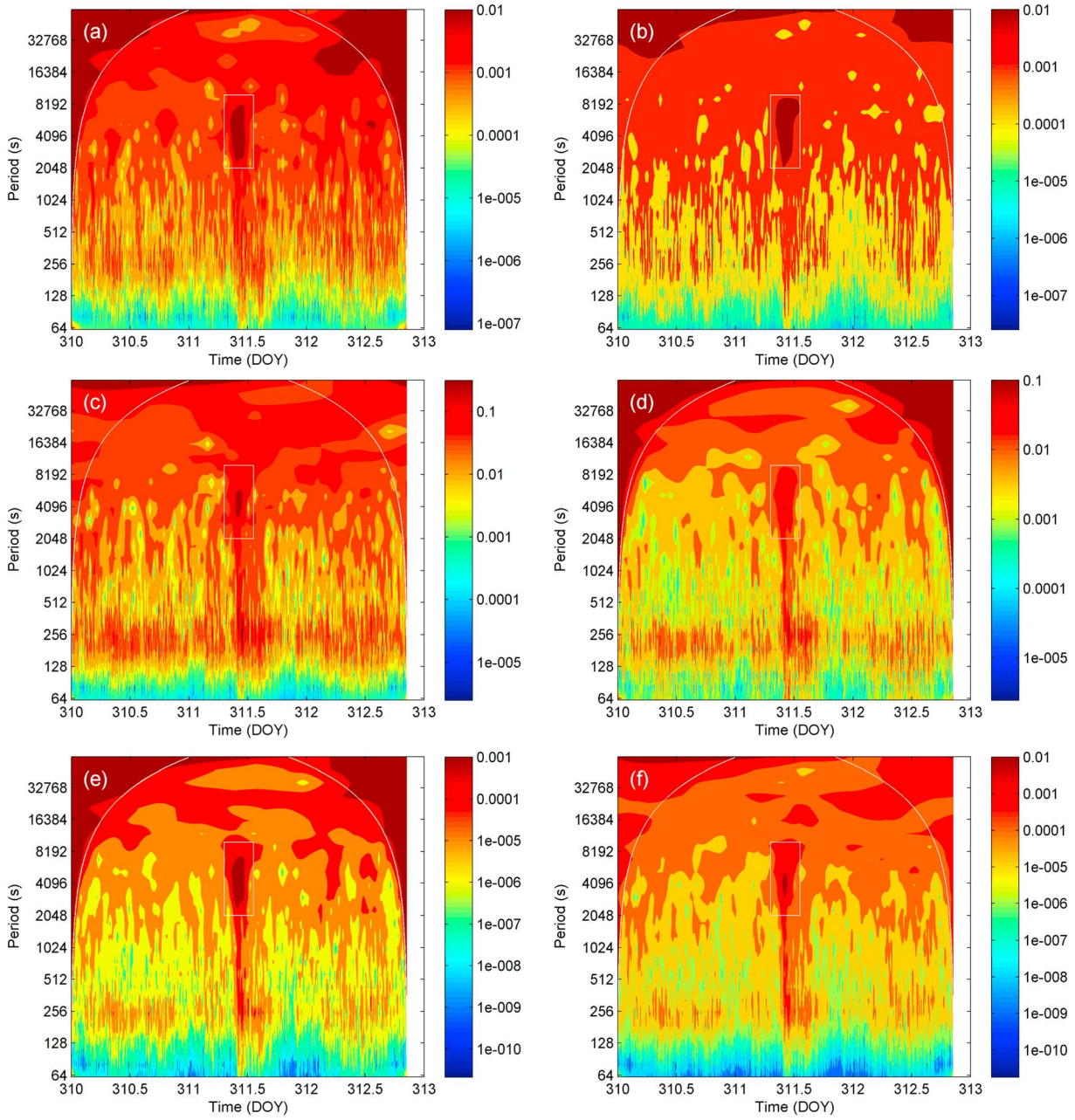


Figure 7. (a) $|\widetilde{u}|$, (b) $|\widetilde{v}|$, (c) $|\widetilde{p}_L|$, (d) $|\widetilde{p}_E|$, (e) $\left|\widetilde{p}_e\widetilde{u}_{||}^*\right|$, and (f) $\left|\widetilde{p}_L\widetilde{u}_{||}^*\right|$. Scale units are ms^{-1}, ms^{-1}, Pa, Pa, Pa ms^{-1}, and Pa ms^{-1}, respectively. In each panel the white curve shows the COI region edge and the large mountain wave event is indicated by the white box.

Because of the observed intermittent nature of gravity waves as wave packets, we assume they can be described as Morlet wavelets. All time series $\left(u', v', p_L', p_E', \zeta_b'\right)$ are decomposed using the continuous complex Morlet wavelet transform [*Torrence and Compo*, 1998] (referred to as TC98 hereafter). The Morlet wavelet basis is chosen with nondimensional frequency (ω_0) of 6, in order to satisfy the admissibility condition so that the wavelet transform is reversible and so as to be able to infer wave amplitudes from the CWT (Continuous Wavelet Transform). As shown in Figures 1b and 1c, there are some data gaps in the time series during the flights. We use a linear interpolation method to fill the missing values when the gaps are less than 600 s and break the time series into different segments that are analyzed separately when the gaps are larger than 600 s. In order to get reliable results, time series with lengths shorter than 19 h are discarded in the gravity wave parameter retrievals. Wavelet frequencies corresponding to periods ranging from 60 s to 19 h are used in the wavelet transform, since a gravity wave packet may project onto wavelets with frequency outside of

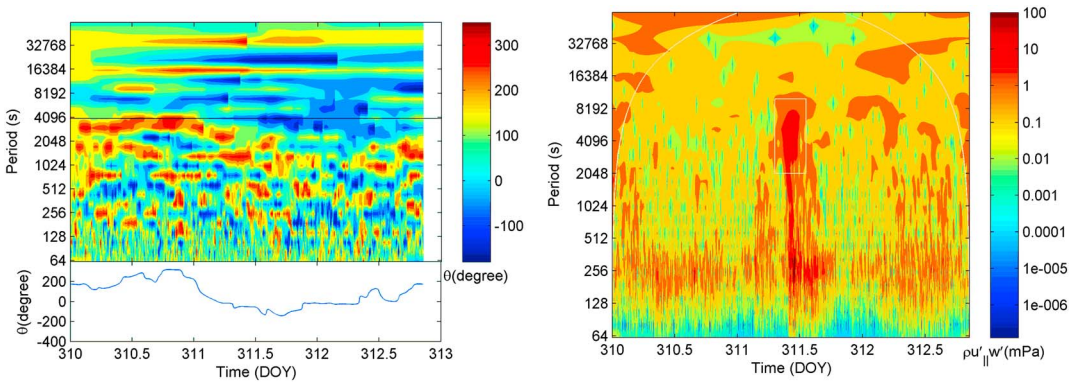


Figure 8. (top left) The propagation direction in each time-(intrinsic) frequency bin; (bottom left) Cross section at period (~1.1 h) indicated by the black line in the top panel; (right) Density-weighted absolute momentum flux in each time-(intrinsic) frequency bin. Note the log scale.

the gravity wave band. However, the momentum flux will only be calculated for the range of frequencies lower than *N*. The derived wavelet coefficients represent the amplitude and phase of the decomposed signal in time-(intrinsic) frequency space and are denoted with tildes, e.g., $\tilde{u}(t_i, \hat{\omega}_j)$ corresponds to the decomposed zonal velocity perturbation time series at time t_i and the *j*th wavelet with central frequency of $\hat{\omega}_j$. The scale resolution (δj) is selected to be 0.4, which corresponds to decomposition into 26 wavelets according to equation (3) (TC98):

$$J = \delta j^{-1} \log_2(s_J/s_0), \tag{3}$$

where s_0 and s_J are 60 s and 19 h, respectively, in this calculation. The scale resolution is kept the same in the wavelet analysis for all segments of the time series. The coefficients are then normalized using a delta (δ) wavelet function as described in section 3i in TC98 so that the time series can be reconstructed with accurate amplitude and to ensure that the total energy is conserved under the wavelet transform.

An example of the modulus of the wavelet coefficients for the perturbation values of $|\tilde{u}|$, $|\tilde{v}|$, $|\tilde{p}_L|$, $|\tilde{p}_E|$, $\left|\tilde{p}_E \tilde{u}_{||}^*\right|$, and $\left|\tilde{p}_L \tilde{u}_{||}^*\right|$ is shown in Figure 7 for the 3 day time period corresponding to the balloon passage over the Antarctic Peninsula of Figure 5. Here $\tilde{u}_{||}^*$ denotes the complex conjugate of $\tilde{u}_{||}$, where $\tilde{u}_{||}$ is the velocity components parallel to the wave propagation direction. All of the parameters shown in Figure 7 will be used in the later momentum flux and phase speed calculations. Generally, the modulus of the coefficient increases as the wavelet period increases for each variable. However, the orographic gravity waves generated by the Antarctic Peninsula show up clearly in each velocity component and pressure variable with a maximum at a wave period of about 1–2 h around the midday on DOY 311 as indicated by the white box in each panel of Figure 7. Large values can also be found at near the buoyancy frequency with a period of ~300 s, especially for the pressure and momentum terms in Figures 7c to 7f.

To avoid interpreting noise as GWs, wavelet coefficients for which the modulus is smaller than 3 times the STD of the observation uncertainties are set to zero in the momentum flux calculation. STD values for (u, v, ζ_b, and p_L) are set to be (0.005 ms^{-1}, 0.005 ms^{-1}, 0.2 m, and 0.1 Pa) for PPPAR solution and (0.05 ms^{-1}, 0.05 ms^{-1}, 5 m, and 0.1 Pa) for RTP solution. The cone of influence (COI) region is also set to zero in the momentum flux calculation to avoid the artifact edge effects in the wavelet transform (TC98), as, for example, seen clearly in the large coefficient values in the top (low frequency) corners of each panel of Figure 7.

The gravity wave propagation direction $\theta(t_i, \hat{\omega}_j)$ (counterclockwise from east) is found by geometrically rotating each $(\tilde{u}, \tilde{v})$ using a principle component analysis so as to find the largest variance on the rotated direction, retaining a 180° ambiguity in $\theta(t_i, \hat{\omega}_j)$ (see B08 and VH14 for more details). $\tilde{u}_{||}$ and $\hat{u}_{\perp}$are the velocity components parallel and perpendicular to the propagation direction. An example of the propagation direction in each time-(intrinsic) frequency bin as well as the cross section at the wavelet period of ~1.1 h are shown in Figure 8. A high variability of propagation directions is evident, especially for short periods, but the coherent direction for the gravity waves upstream and downstream of the peninsula is clear at ~1.3 h period.

The density-weighted vertical momentum flux of the gravity waves can be related to the balloon observations by (B08):

$$\overline{\rho}\mathrm{Re}\left(\widetilde{u}_{||}^{*}\widetilde{w}\right) = -\frac{\hat{\omega}_j}{H\hat{N}}\mathrm{Im}\left(\widetilde{p}_L\widetilde{u}_{||}^{*}\right) \tag{4}$$

where Re() and Im() stand for the real part and imaginary part of the complex quantities. H is the density scale height calculated from a 3 day average of ERA-Interim lapse rate held constant for the entire flight. Only the real part of the moment flux is relevant, namely, $\mathrm{Re}\left(\widetilde{u}_{||}^{*}\widetilde{w}\right)$, because the imaginary part will vanish when averaged over a wave period. We calculate the density-weighted vertical momentum flux at each time-(intrinsic) frequency bin (as shown in Figure 7b) according to equation (4) from the pressure and rotated balloon velocities assuming H is 6.45 km. We also calculate the zonal and meridional components of the density-weighted momentum flux by multiplying by $\cos\left(\theta\left(t_i,\hat{\omega}_j\right)\right)$ and $\sin\left(\theta\left(t_i,\hat{\omega}_j\right)\right)$.

The intrinsic phase speed of the gravity wave $\hat{c}$ can be inferred from the polarization relationship [*Fritts and Alexander*, 2003] and estimated directly at each time-(intrinsic) frequency bin from the Eulerian pressure perturbation:

$$\hat{c} = \frac{1}{\overline{\rho}\delta}\frac{\mathrm{Re}\left(\widetilde{p}_E\widetilde{u}_{||}^{*}\right)}{\widetilde{u}_{||}^{2}}, \tag{5}$$

where $\delta = 1 - \frac{\hat{f}^2}{\hat{\omega}_j^2}$..

In order to estimate the phase speed and propagation direction of individual gravity wave packets, their central frequency must be identified. Each wave packet can project onto several wavelets and there may be several wave packets present at one time. A number of wave packets, k, with central frequencies, denoted as $\left[\hat{\omega}_k^c(t_i)\right]_k$ may be identified in the frequency range from f to 0.5 N at one observation time t_i, by identifying all local maxima in the momentum flux at that time. The envelopes of the wave packets are then identified by selecting the neighboring frequencies within the range of 1/19 h^{-1} to 0.5 N for which the vertical momentum flux is greater than 10% of the central frequency.

$$\mathrm{Re}\left[\widetilde{u}_{||}^{*}\widetilde{w}\left(t_i,\hat{\omega}_j\right)\right] \geq \frac{\mathrm{Re}\left[\widetilde{u}_{||}^{*}\widetilde{w}\left(t_i,\hat{\omega}_k^c(t_i)\right)\right]}{10}. \tag{6}$$

Here $\hat{\omega}_j^{gw}(t_i)$ now indicates the frequencies j that are included in any identified wave packet. The absolute GW momentum flux at time t_i is computed by summing over the selected frequencies contained in all of the gravity wave packets present at that time:

$$\sum_j \overline{\rho}\mathrm{Re}\left\{\widetilde{u}_{||}^{*}\widetilde{w}\left[t_i,\hat{\omega}_j^{gw}(t_i)\right]\right\}. \tag{7}$$

The high frequency and low frequency portions of the absolute GW momentum flux at time t_i are also calculated from equation (7) separately over the two frequency bands. The flight-mean momentum flux is then calculated in each geographic bin by taking the mean of all time points when the balloon passed through the bin, equivalent to averaging over time. Note that we truncate the high frequency wave packets at a frequency of 0.5 N, which will exclude some wave packets with frequency content higher than 0.5 N. This is done to avoid the issues highlighted in VH14 where the balloons go off their isopycnic surfaces at frequency higher than ~0.5 N.

Initial estimates of the phase speed and momentum flux are calculated assuming upward vertical propagation. To examine the distribution of phase speeds represented in the gravity wave packets that include upward and downward propagation, the 180° ambiguity of the propagation direction is resolved in the following way. Assuming a perfect isopycnic balloon (equations (28) and (29) in VH14) the sign of the vertical wave number m can be determined from the balloon observations:

$$\mathrm{sign}(m) = -\mathrm{sign}\left(\mathrm{Im}\left(\widetilde{\zeta}_b\widetilde{p}_L^{*}\right)\right). \tag{8}$$

This is calculated at each time-(intrinsic) frequency bin. If vertical propagation is determined to be downward, i.e., vertical wave number $m > 0$, then $\theta\left(t_i,\hat{\omega}_j\right)$ is rotated by 180°, changing the direction of the phase speed,

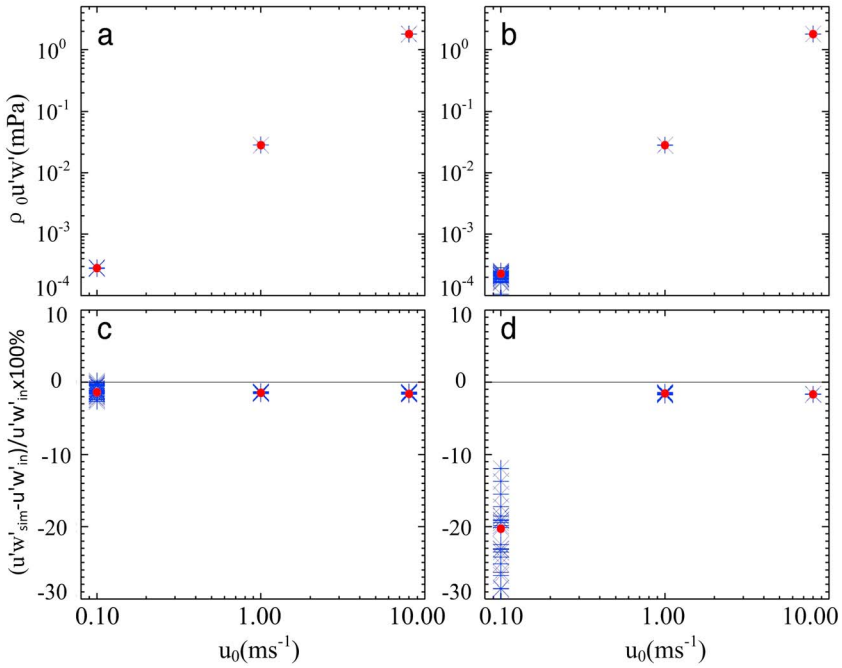


Figure 9. (a) Values of momentum flux in mPa plotted as a function of wave packet amplitude, u_0. The blue star symbols represent the retrieved momentum flux with PPPAR noise added (0.005 ms^{-1} in horizontal velocities) and the red symbols show the retrieved values without noise. (b) Similar to Figure 9a but with higher noise (0.025 ms^{-1} in horizontal velocities) added. (c) The percentage of the difference between the retrieved and input values w.r.t. the input values for the low noise case (Figure 9a). (d) The percentage difference for the high noise case (Figure 9b).

and the sign of the momentum flux is also reversed. The intrinsic phase speed is assigned to the frequencies representative of the wave packet envelope after the packet identification to describe the distribution of $\left[\theta\left(t_i,\hat{\omega}_k^c(t_i)\right),\hat{c}\left(t_i,\hat{\omega}_k^c(t_i)\right)\right]$ and then the momentum flux associated with the individual wave packet $\overline{\rho}\mathrm{Re}\left[\widetilde{u}_{||}^{*}\widetilde{w}\left(t_i,\hat{\omega}_k^c(t_i)\right)\right]$ is integrated over the frequencies contained in the packet.

5.2. Simulation Comparison

The uncertainties of the instruments carried on the SPBs will set a noise floor, below which the gravity wave parameters cannot be reliably retrieved. In order to test which part of wave packets will be mostly affected by the balloon position accuracy, a series of simulations were conducted using the methodology described in VH14, where a wave packet of a wave with frequency $\hat{\omega}$ and a Gaussian envelope of the form

$$u'_{||}=u_0e^{-t^2/2\sigma^2}\cos(\hat{\omega}t) \tag{9}$$

was used. Thirty realizations of noise were added to simulated wave packets with amplitude, u_0, set to 0.1, 1, and 8 ms^{-1}, respectively. Here the simulated values of $\hat{\tau}=60$ min, $\hat{\omega}=2\pi/\hat{\tau}$, $\hat{c}=40$ ms^{-1}, and $\theta=300°$ were used. The retrieved results are shown in Figure 9. Figures 9a and 9c show momentum flux retrievals for packets with the PPPAR velocity errors (0.005 ms^{-1}) added and Figures 9b and 9d are with the velocity errors assumed in VH14 added. Note VH14 assumed 0.75 m and 0.025 ms^{-1} position and velocity errors, but we showed that the magnitude of the RTP horizontal position errors are about 5 m and velocity errors are around 0.05 ms^{-1} (PSC18) and 0.1 ms^{-1} (PSC19). In the best case, filtering out high frequency spikes (higher than buoyancy frequency) due to RTC offsets, the realistic RTP velocity errors are closer to 0.035 ms^{-1} and 0.060 ms^{-1}. The red stars in Figure 9 are the retrievals where there are no errors added in either case. Ignoring the small offsets, the noise levels of the PPPAR solutions show much smaller dispersion and bias in retrieving momentum fluxes at small amplitudes than results with assumed errors from VH14 added. Waves with small amplitudes will likely break higher up in the atmosphere and therefore are important for momentum transfer to the upper middle atmosphere. The PPPAR solutions provide the opportunity to estimate fluxes for packets with much lower amplitudes than is presently possible.

5.3. Gravity Wave Parameter Comparison Results

We have estimated the terms that contribute directly to the momentum flux (horizontal velocities) and intrinsic phase speed (horizontal velocities and vertical position) in Figures 3 and 4 in order to assess the impact of the improved positions over the RTP solutions. The mean Eulerian pressure differences between PPPAR and RTP solutions of −8.23 Pa for PSC18 (Figure 3) and −8.70 Pa for PSC19 (Figure 4) are attributed to the difference in GPS antenna location height on the balloons. The STD Eulerian pressure perturbation differences are 5.56 Pa and 5.70 Pa, respectively, which are equivalent to the scaled values of altitude differences because of the relationship given by equation (2). All the mean values of the differences including the velocity and Eulerian pressure are removed in the wavelet analysis, producing no impacts on the GW parameter retrieval. Following the wavelet decomposition method described previously, the momentum flux and intrinsic phase speed are retrieved from both the PPPAR and RTP solutions and the differences between these retrievals are calculated to study the improvement contributed by the high-accuracy GPS receivers in a real world situation.

The geographical distribution of the density-weighted absolute momentum fluxes in the wave propagation direction is shown in 10°× 5° latitude-longitude bins in Figure 10 (top row). There are usually one to three balloon passes in each bin, with an average of 988 measurements per bin. Hot spots can be seen in the vicinity of the Antarctic Peninsula, the ridge of Wilkes Land (~110°E) and the Mac. Robertson Land (~60°E) from both results based on the PPPAR and RTP solutions. Density-weighted momentum fluxes can reach ~80 mPa in the most active areas of the Antarctic Peninsula, a value which is ~10 times larger than the average value of ~8 mPa over the entire sampled Southern Hemisphere (SH) during this time period. The average value measured during the previous Vorcore campaign was 2.5 mPa because a significant portion of the higher frequency momentum flux was not observed. The smallest values are observed over the Antarctic plateau from 0 to 90° east with momentum fluxes below 5 mPa, although this region is not well sampled by these particular balloons. Areas of slightly higher momentum flux activity can be found over oceanic regions, principally north of the Atlantic coastline. Waves in this region have been identified historically as both nonorographic waves generated locally and orographic gravity waves advected downwind from the peninsula [*Hindley et al*., 2015; *Jewtoukoff et al*., 2015]. Although mountain waves from remote islands have been observed in past studies [*Alexander and Grimsdell*, 2013; *Hoffmann et al*., 2013], the data set used in this study does not sample the small oceanic islands, indicating the sources are primarily from locally nonorographic origin or are of orographic origin from peninsula. *Jewtoukoff et al*. [2015] associated the nonorographic gravity waves observed at the latitude of storm tracks with midlatitude jets and fronts and geostrophic adjustment. Most of differences between the two solutions (PPPAR minus RTP) are found to be positive, indicating an underestimation of momentum fluxes from the RTP solutions, which is mainly due to the larger noise threshold values used for RTP solutions. There are only a few bins, mainly over the coastlines, where the differences are negative (overestimated by RTP), and we attribute these to random errors. The mean value of the momentum flux differences over the entire area covered by the two balloons is ~0.56 mPa and the RMS deviation is about 0.74 mPa, which is ~8% of intrabin variations before differencing (~9.79 mPa for PPPAR and ~9.84 mPa for RTP). In Figures 10–12, bins with poor statistical significance are indicated with black dots, based on the balloon path sampling less than 50% of the latitudinal width of the bin.

The density-weighted zonal momentum fluxes are presented in Figure 10 (middle row). The zonal momentum fluxes are found to be negative almost everywhere, showing the gravity waves propagate against the mean eastward flow in the SH springtime stratosphere, which is consistent with the results from observations from the previous campaign in Antarctica in 2005 [*Vincent et al*., 2007]. Not surprisingly, the zonal momentum flux hot spots are also observed in those areas with large absolute momentum flux, reaching nearly ~ −50 mPa over the Antarctic Peninsula and ~ −15 mPa along the Indian Ocean coastline. Moderately large values of ~ −10 mPa can be seen in the southern Atlantic region contributed by nonorographic sources. Mean values of density-weighted zonal momentum fluxes are ~ −3.09 mPa and ~ −2.32 mPa based on PPPAR solutions and RTP solutions, respectively. The mean difference is around −0.76 mPa with RMS deviation reaching ~1.36 mPa which is ~25% of intrabin variations of zonal momentum fluxes (5.61 and 5.30 mPa for PPPAR and RTP) before differencing.

In contrast to the zonal momentum fluxes, the campaign averaged density-weighted meridional momentum fluxes in Figure 10 (bottom row) are significantly smaller in magnitude. Again, the most active area found in the meridional momentum flux, exceeding 43 mPa, is over the Antarctic Peninsula. However, the hot spots

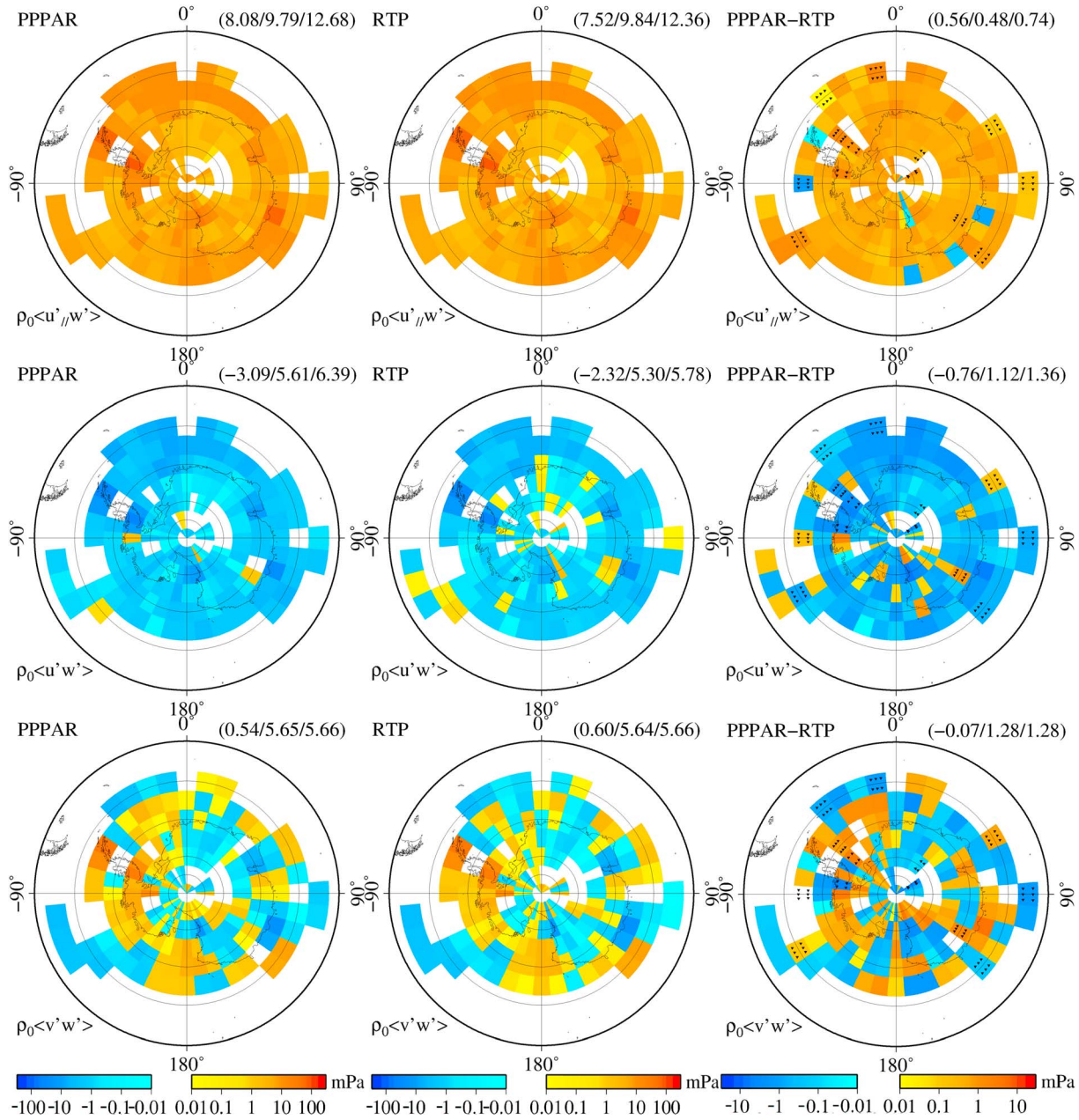


Figure 10. Comparison of the geographic distribution of density-weighted momentum fluxes derived from (left column) PPPAR and (middle column) RTP solutions and (right column) their difference (PPPAR-RTP). Absolute, zonal, and meridional momentum flux results are shown in Figures 9 (top row) to 9 (bottom row). The color scales have been divided by a factor of 10 for the right most column compared with the left two columns. Values given in the brackets at the top right of each panel are the mean value, the standard deviation and the RMS values in all bins, respectively. Bins in the right most columns filled with black dots denote statistical insignificance due to insufficient measurements.

along the Indian Ocean coastline are opposite in sign to the zonal component. Mean values of the PPPAR and RTP solution-derived meridional momentum fluxes are approximately 0.54 mPa and 0.60 mPa, with standard deviation of ~5.65 and 5.64 mPa and the difference is ~ −0.07 mPa with an RMS of ~1.28 mPa (~23% of the PPPAR intrabin variations).

According to equation (4), it is the time differences of horizontal positions, i.e., the horizontal velocities, rather than the absolute horizontal positions that are used in the momentum flux estimation. As can be seen from the zoomed time series in Figures 3 and 4, the horizontal position errors in RTP solutions between the clock resets vary quite systematically with time, which induces small systematic velocity errors between two spikes.

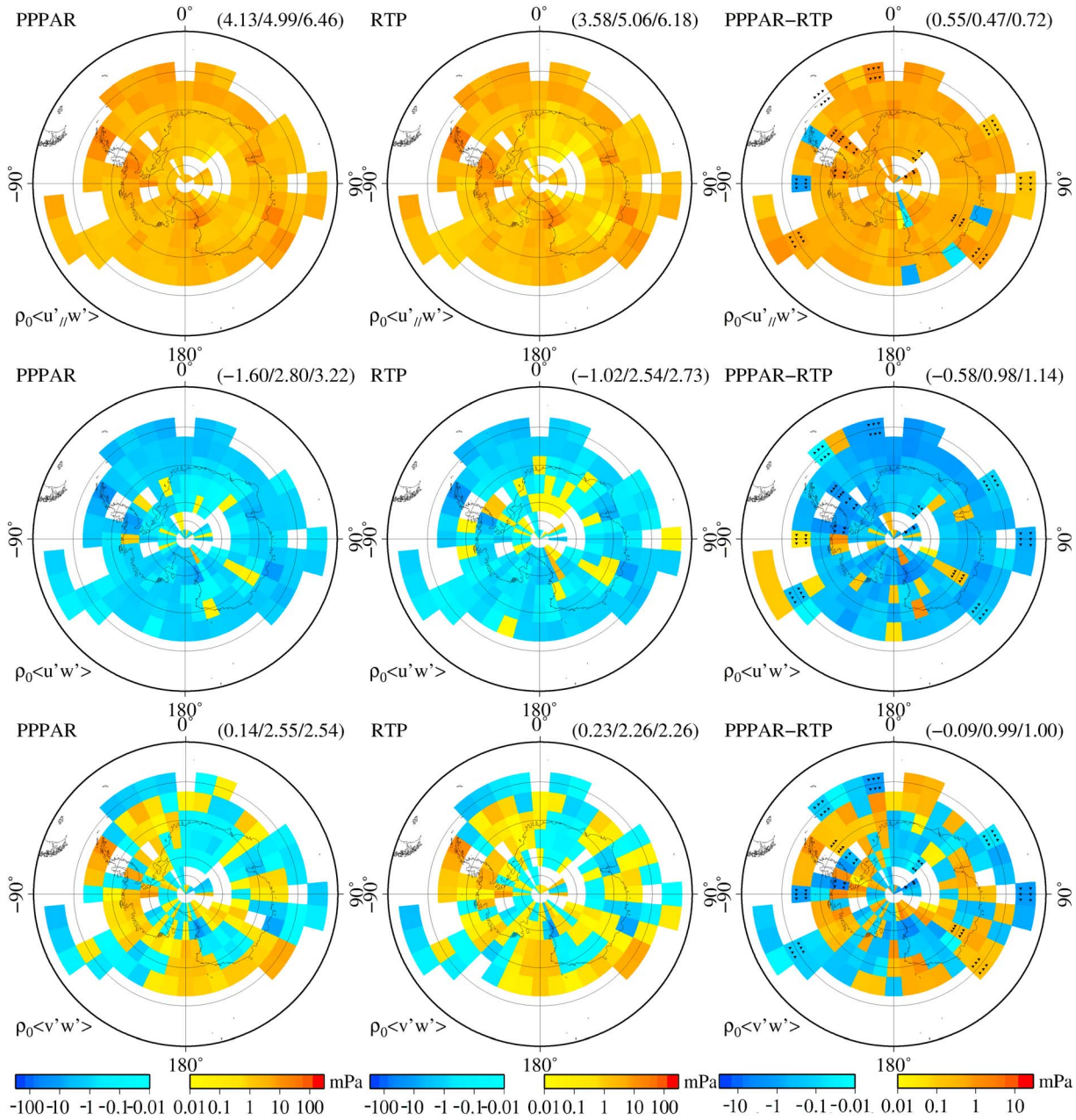


Figure 11. Comparison of the geographic distribution of density-weighted momentum fluxes for the high frequency portion of GWs (intrinsic period shorter than 1 h) derived from (left column) PPPAR and (middle column) RTP solutions and (right column) their difference (PPPAR-RTP). Absolute, zonal, and meridional momentum flux results are shown in Figures 11 (top row) to 11 (bottom row). The color scales have been divided by a factor of 10 for the right most column compared with the left two columns. Values given in the brackets at the top right of each panel are the mean value, the standard deviation and the RMS values in all bins, respectively. Bins in the right most columns filled with black dots denote statistical insignificance due to insufficient measurements.

They are, however, estimated to be insignificant. The discontinuous velocity spikes with frequency higher than the buoyancy frequency will be filtered out in the wavelet analysis and only those parts with frequency ranging from ~1/30 min^{-1} to 0.5 *N* will impact on the high frequency gravity wave momentum flux retrievals.

The retrieved momentum fluxes are divided into a high frequency portion, which are typically parameterized in global circulation models (GCMs), corresponding to periods shorter than 1 h, and a low frequency portion for periods longer than 1 h. Results are presented in Figures 11 and 12, respectively. *Jewtoukoff et al*. [2015] argued that the Concordiasi results should be greater by a factor of 2 than previous results from the Vorcore by including higher frequencies. The PPPAR results confirm that the mean absolute momentum flux

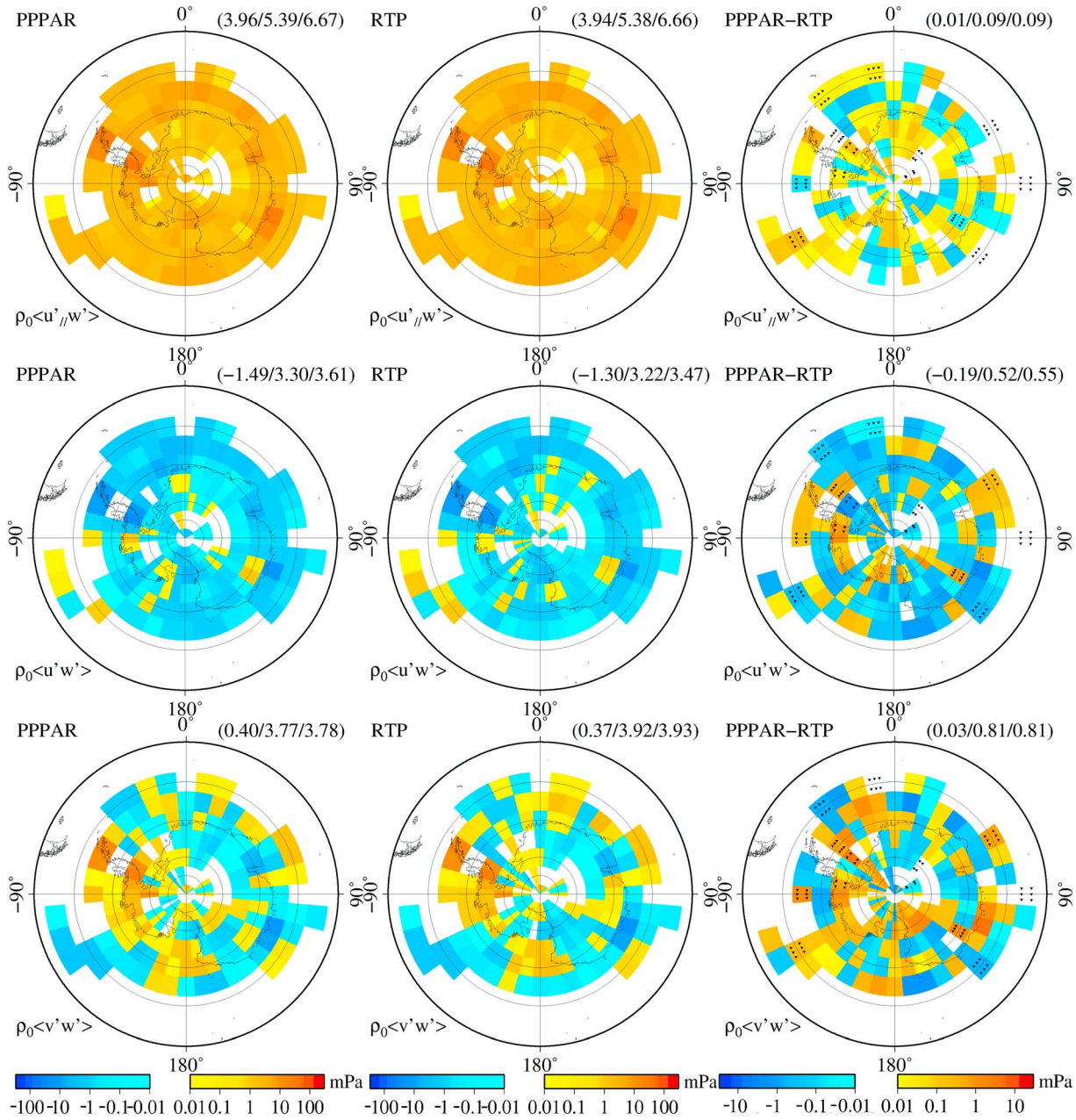


Figure 12. Comparison of the geographic distribution of density-weighted momentum fluxes for the low frequency portion of GWs (intrinsic period greater than 1 h) derived from (left column) PPPAR and (middle column) RTP solutions and (right column) their difference (PPPAR-RTP). Absolute, zonal, and meridional momentum flux results are shown in Figures 12 (top row) to 12 (bottom row). The color scales have been divided by a factor of 10 for the right most column compared with the left two columns. Values given in the brackets at the top right of each panel are the mean value, the standard deviation and the RMS values in all bins, respectively. Bins in the right most columns filled with black dots denote statistical insignificance due to insufficient measurements.

for high and low frequencies are comparable, 4.13 mPa and 3.96 mPa, respectively. Mean values of differences are 0.55, −0.58, and −0.09 at high frequency and 0.01, −0.19, and 0.03 at low frequency for absolute, zonal, and meridional momentum fluxes, respectively. The RMS of the absolute total momentum flux differences between the PPPAR and RTP solutions is only 0.09 mPa in the low frequency portion but ~0.72 mPa for the high frequency portion, which are ~2% and ~15% of PPPAR intrabins variations, respectively. The RMS of zonal momentum flux differences are 0.55 and 1.14 mPa in the low frequency and high frequency portions, respectively, around 16% and 41% of values before differencing. The RMS of meridional momentum flux differences are 0.81 and 1.00 mPa, reaching ~21% and 40% of flux intrabin variations based on PPPAR solutions.

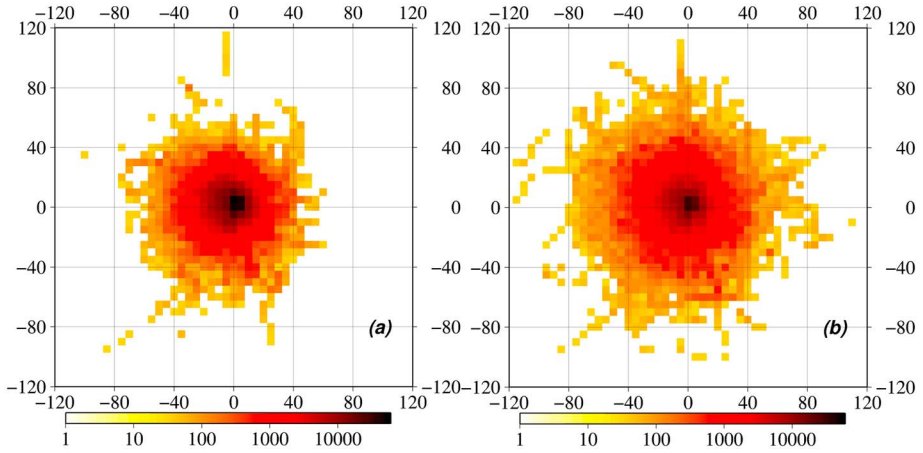


Figure 13. Distributions of gravity wave packet number density as a function of intrinsic phase speed derived from (a) PPPAR and (b) RTP solutions. Horizontal and vertical axes denote $\hat{c}_x$ and $\hat{c}_y$ in ms^{-1}, respectively. Color scales denote the number of wave packets.

Apparently, the improvements of PPPAR positioning benefit the momentum flux retrieval much more for the high frequency GWs than the low frequency GWs. This is particularly significant for the meridional momentum flux because the size of the differences (RMS 1.00 mPa) are about 5 times greater than the campaign averaged momentum flux (0.14 mPa) and ~40% of the intrabin variations. The meridional momentum flux hot spots appear to be associated with areas of strong topographic contrast at the coastline, which may also be affected by katabatic flow, and the differences between PPPAR and RTP in these locations can be as much as 5 mPa.

Intrinsic phase speeds are estimated for each of the wave packets and assigned to the center frequency of the wave packet. The distributions of gravity wave packet number density as a function of zonal intrinsic phase speed ($\hat{c}_x$) and meridional phase intrinsic phase speed ($\hat{c}_y$) are plotted in Figure 13. The distribution based on the PPPAR solutions is more concentrated near zero phase speed than that based on the RTP solutions, indicating an overestimation of intrinsic phase speed from the RTP solutions. The distributions are quite symmetric around zero. In Figure 14, the distribution of the zonal momentum flux as a function of ($\hat{c}_x$,$\hat{c}_y$) is presented. There is considerable difference in the spread of the distribution of zonal momentum flux between the PPPAR and RTP solution results. The PPPAR results are more compact, indicating once again possible overestimation of momentum flux at greater phase speed in the RTP results and underestimation of momentum flux at lower phase speed. This was anticipated in an assessment of the method in *Hertzog et al*. [2008]. The high negative values with westward propagation in the upper left quadrant Figure 14a

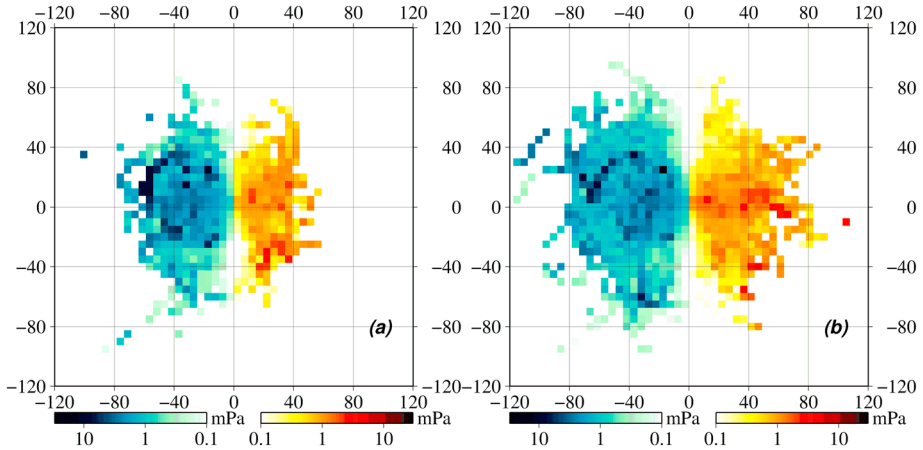


Figure 14. Distributions of zonal momentum fluxes as a function of intrinsic phase speed derived components $\hat{c}_x$ and $\hat{c}_y$ derived from (a) PPPAR and (b) RTP solutions. Negative momentum flux (westward propagation) is shown in blue, while the red scale denotes positive flux (eastward propagation).

are also found in Figure 14b. However, some hot spots near ($\hat{c}_x = -30\ \mathrm{ms}^{-1}$ and $\hat{c}_y = 20\ \mathrm{ms}^{-1}$) in Figure 14a do not appear in Figure 14b where the PPPAR results have greater amplitude. In addition, Figure 14b shows high values of momentum flux associated with eastward propagation at phase speed greater than $40\ \mathrm{ms}^{-1}$. The feature is not found in the PPPAR results in Figure 14a.

Parameterizations of the GW drag in GCMs often use an exponential distribution of gravity wave sources with a characteristic momentum flux (F_m) and intrinsic phase speed ($\hat{c}_p$) [*Hertzog et al.*, 2008; *Alexander and Dunkerton*, 1999], for example,

$$F(\hat{c}_{x/y}) = F_m \mathrm{sign}(\hat{c}_{x/y}) \exp\left(-\frac{|\hat{c}_{x/y}|}{\hat{c}_p}\right), \tag{10}$$

where $F(\hat{c}_{x/y})$ denotes zonal or meridional momentum flux. Fitting an exponential to the broader distribution seen in Figure 14 for the RTP results would have higher characteristic phase speed than for the PPPAR results and lower momentum flux at low phase speeds. This confirms the suggestion in *Hertzog et al.* [2008] that the flux was previously underestimated at low phase speeds. This affects the height in the middle atmosphere where the parameterized GW momentum is deposited by wave breaking and thus affects the mean thermodynamic state of the middle atmosphere and global mean flow in the GCMs.

6. Discussion and Conclusions

The 19 superpressure balloons launched in the Concordiasi field campaign over Antarctica from September 2010 to January 2011 provide a unique means of measuring gravity wave characteristics as a function of intrinsic frequency. The Antarctic polar vortex provides ideal conditions for balloons drifting in the lower stratosphere to provide good coverage over this region, with continuous sampling that makes it possible to evaluate the intermittency of GW activity as well as momentum flux. The high sample rate of the GPS receivers carried on the balloons enables us to study the entire gravity wave frequency range compared to previous campaigns, and better positioning accuracy makes it possible to estimate the vertical displacement directly rather than infer the effect of vertical displacement from the pressure measurements.

Two of the 19 balloons also carried high-accuracy dual-frequency GPS receivers initially designed for the purpose of GPS radio occultation research. Compared to the single-frequency GPS receiver on each balloon, the high-accuracy receivers enable us to significantly improve the estimated balloon position accuracy with the PPPAR GPS postprocessing analysis method. Two high-accuracy receivers with constant distance between the antennas were deployed on PSC18 in order to investigate the motion of the balloon platform and provided an independent method to evaluate the position precision estimated from the PPPAR method. The PPPAR method derived positions with precision better than 0.1 m in the horizontal and 0.2 m in the vertical.

In order to evaluate the impact of the improved positions from the PPPAR method on the final determination of gravity wave momentum flux and phase speed retrievals, the time series of 3-D positions, horizontal velocities and Eulerian pressure perturbations derived from high-accuracy receivers are compared with the results from the single-frequency GPS receiver for the two balloons for the entire duration of the flights. Due to the inaccurate time tagging of the position data by the onboard clock (RTC) with ~1 s precision for the single-frequency GPS receiver, the position differences between PPPAR solutions and real-time single-frequency GPS (RTP) solutions turn out to be quite large. The standard deviation is ~3–10 m in the horizontal and ~5 m in the vertical, depending on the velocity of the balloon. These position accuracies are several times worse than the uncertainties assumed in simulations of the accuracy of gravity wave retrievals in *Vincent and Hertzog* [2014]. The standard deviations of horizontal velocity differences for PPPAR and RTP are ~0.05 ms^{-1} to ~0.1 ms^{-1} for PSC18 (the slower balloon) and PSC19 (the faster balloon), and many spikes are found in the differences which can reach near $0.4\ \mathrm{ms}^{-1}$ due to discontinuities in the RTP time series at the RTC reset. The standard deviation of the Eulerian pressure perturbation differences using the PPPAR versus the RTP vertical positions is around 5–6 Pa during the flights. New simulation tests and results from the higher accuracy PPPAR solutions show that the improvement can provide more reliable estimates of fluxes for low amplitude wave packets than is otherwise possible.

Based on the position time series derived from the PPPAR method, one event from a balloon passage over the Antarctic Peninsula is used to examine gravity waves properties associated with the topography through

time series and spectral analysis. Strong fluctuations are found in all time series during the period when the balloon passed over the peninsula. The estimated slopes of the spectra for gravity wave frequencies are −1.95 and −1.97 for zonal velocity and meridional velocity, respectively, and significant departures of the PSD from the power law spectra can be found in the frequencies corresponding to the mountain waves induced by the topography in the Antarctic Peninsula.

The density-weighted momentum fluxes and intrinsic phase speed were retrieved from balloon measurements for the entire flight durations and comparisons made between the results using the PPPAR position solutions and RTP position solutions. Hot spots of momentum fluxes are observed in the vicinity of the Antarctic Peninsula, which shows the largest mean high frequency momentum flux (~37 mPa) among all bins and where instantaneous values as large as ~150 mPa (more than 30 times the mean value) have been observed. Higher momentum fluxes are also found along the coastline of Wilkes Land and Mac. Robertson Land for both data sets, where the momentum fluxes can be several times larger than the mean value and are associated with the topographic wave sources, as also described in *Jewtoukoff et al*. [2015]. Significant momentum fluxes are also found in the southern Atlantic Ocean, which are considerably stronger than areas on the east Antarctic plateau, indicating that nonorographic gravity wave sources are also present. Mean values of the density-weighted absolute, zonal, and meridional momentum fluxes are, respectively, ~8.08, −3.09, and 0.54 mPa from the PPPAR solutions of the two balloon flights. We point out that 8.08 mPa is significantly greater than the ~2.5 mPa average absolute momentum flux estimated from the 2005 Vorcore campaign [*Hertzog et al*., 2008], primarily due to including GWs with periods shorter than 1 h. The mean differences between the PPPAR and RTP solutions were ~0.56, −0.76, and −0.07 mPa with RMS of 0.74, 1.36, and 1.28 mPa. We break up the analysis into the high and low frequencies bands. The RMS of absolute, zonal, and meridional momentum flux differences are ~0.72, 1.14, and 1.00 mPa (~15%, 41%, and 40% of PPPAR-based flux intrabin variations) for the high frequency portion and are ~0.09, 0.55, and 0.81 mPa (~2%, 16%, and %21 of PPPAR-based flux intrabin variations) for waves with intrinsic periods longer than 1 h (low frequency portion). Mean values of differences are 0.55, −0.58, and −0.09 at high frequency and 0.01, −0.19, and 0.03 at low frequency for absolute, zonal, and meridional momentum fluxes, respectively. Both the simulations and balloon observations show that the improvements due to PPPAR positioning particularly benefit momentum flux retrievals for both small amplitude and high frequency gravity waves. We point out that the most significant impact of PPPAR is on the meridional flux at high frequencies, where the differences between PPPAR and RTP have an RMS of 1.00 mPa, which represents variations 5 times the mean meridional flux of 0.14 mPa and ~40% of intrabins variations of ~2.55 mPa. Since these high-frequency GWs will be parameterized in GCMs, the climate model results can be significantly improved due to more precise flux estimates from PPPAR solutions.

Intrinsic phase speeds show significant differences between PPPAR and RTP results due to the relatively large vertical displacement differences. The PPPAR phase speed distributions have more momentum flux at lower phase speeds and less momentum flux at higher phase speeds. Parameterizations of the GW drag in GCMs that use, for example, an exponential distribution with a characteristic intrinsic phase speed [*Hertzog et al*., 2008; *Alexander and Dunkerton*, 1999] will be affected. As theorized in *Hertzog et al*. [2008], these results confirm that the flux was previously underestimated at low phase speeds, which affects the height in the middle atmosphere where the parameterized GW momentum is deposited by wave breaking and thus affecting the global mean flow in the GCMs.

Dual-frequency GPS receivers can record balloon positions with high accuracy. However, they also require a larger storage capability and greater data transmission bandwidth and thus have greater cost than single-frequency receivers. Based on the discussion here, we have quantified the improvement produced by better GPS receivers and the absolute accuracy of the single-frequency GPS receivers, as well as the corresponding impacts on important gravity wave parameters. This will provide valuable information for planning equipment in the future campaigns for the purpose of gravity wave research.

Acknowledgments

This work was supported by NSF grants 0814290, ANT-1043676, and ANT-1261680. W. Zhang is supported by China Scholarship Council (201406270066). We thank the following people and organizations for their support: NSF Office of Polar Programs for the instrument deployment field support; F. Rabier at ECMWF and P. Cocquerez (CNES) for encouraging the integration of this research into the Concordiasi research program; P. Wyss, J. Zimmerman and M. Everly at the Purdue University AMY Chemistry Facility for assistance with receiver development; A. Johnson for assistance in data collection, P. Cocquerez, M. Minois, O. Gallien, J.-M. Nicot, and the team at CNES for assistance with the GPS ROC deployment. Concordiasi was built by an international scientific group supported by the following agencies: Météo-France, CNES, CNRS/INSU, NSF, National Center for Atmospheric Research (NCAR), University of Wyoming, Scripps Institution of Oceanography, University of Colorado, the Alfred Wegener Institute, the Met Office, and ECMWF. Concordiasi also benefited from logistic or financial support of the operational polar agencies IPEV, PNRA, USAP, and BAS and from BSRN measurements at Concordia. Concordiasi is part of the THORPEX-IPY cluster within the International Polar Year effort. Data collected in the Concordiasi campaign are available on the website "http://igpppublic.ucsd.edu/~jhaase/airborne_ro/2010.251_concordiasi/."

References

Alexander, M. J., and T. J. Dunkerton (1999), A spectral parameterization of mean-flow forcing due to breaking gravity waves, *J. Atmos. Sci.*, *56*, 4167–4182.

Alexander, M. J., and A. W. Grimsdell (2013), Seasonal cycle of orographic gravity wave occurrence above small islands in the Southern Hemisphere: Implications for effects on the general circulation, *J. Geophys. Res. Atmos.*, *118*, 11,589–11,599, doi:10.1002/2013JD020526.

Alexander, M. J., and L. Pfister (1995), Gravity wave momentum flux in the lower stratosphere over convection, *Geophys. Res. Lett.*, *22*, 2029–2032, doi:10.1029/95GL01984.
Alexander, M. J., et al. (2008), Global estimates of gravity wave momentum flux from High Resolution Dynamics Limb Sounder observations, *J. Geophys. Res.*, *113*, D15S18, doi:10.1029/2007JD008807.
Alexander, M. J., et al. (2010), Recent developments in gravity wave effects in climate models and the global distribution of gravity wave momentum flux from observations and models, *Q. J. R. Meteorol. Soc.*, *136*, 1103–1124.
Allen, S. J., and R. Vincent (1995), Gravity wave activity in the lower atmosphere: Seasonal and latitudinal variations, *J. Geophys. Res.*, *100*, 1327–1350, doi:10.1029/94JD02688.
Andrews, D. G., J. R. Holton, and C. B. Leovy (1987), *Middle Atmosphere Dynamics*, 489 pp., Academic, Orlando, Fla.
Bacmeister, J. T., M. R. Schoeberl, L. R. Lait, P. A. Newman, and B. Gary (1990), ER-2 mountain wave encounter over Antarctica: Evidence for blocking, *Geophys. Res. Lett.*, *17*, 81–84, doi:10.1029/GL017i001p00081.
Baumgaertner, A. J. G., and A. J. McDonald (2007), A gravity wave climatology for Antarctica compiled from Challenging Minisatellite Payload/Global Positioning System (CHAMP/GPS) radio occultations, *J. Geophys. Res.*, *112*, D05103, doi:10.1029/2006JD007504.
Boccara, G., A. Hertzog, R. Vincent, and F. Vial (2008), Estimation of gravity-wave momentum fluxes and phase speeds from quasi-Lagrangian stratospheric balloon flights. 1: Theory and simulations, *J. Atmos. Sci.*, *65*, 3042–3055.
Boehm, J., R. Heinkelmann, and H. Schuh (2007), Short note: A global model of pressure and temperature for geodetic applications, *J. Geod.*, *81*, 679–683.
Cao, B., and A. Z. Liu (2016), Intermittency of gravity wave momentum flux in the mesopause region observed with an all-sky airglow imager, *J. Geophys. Res. Atmos.*, *121*, 650–663, doi:10.1002/2015JD023802.
Charron, M., E. Manzini, and C. D. Warner (2002), Intercomparison of gravity wave parameterizations: Hines Doppler-spread and Warner and McIntyre ultra-simple schemes, *J. Meteorol. Soc. Jpn.*, *80*, 335–345.
Dörnbrack, A., T. Birner, A. Fix, H. Flentje, A. Meister, H. Schmid, E. V. Browell, and M. J. Mahoney (2002), Evidence for inertia-gravity waves forming polar stratospheric clouds over Scandinavia, *J. Geophys. Res.*, *107*(D20), 8287, doi:10.1029/2001JD000452.
Eckermann, S. D., and P. Preusse (1999), Global measurements of stratospheric mountain waves from space, *Science*, *286*, 1534–1537.
Ern, M., P. Preusse, M. J. Alexander, and C. D. Warner (2004), Absolute values of gravity wave momentum flux derived from satellite data, *J. Geophys. Res.*, *109*, D20103, doi:10.1029/2004JD004752.
Fritts, D. C., and M. J. Alexander (2003), Gravity wave dynamics and effects in the middle atmosphere, *Rev. Geophys.*, *41*(1), 1003, doi:10.1029/2001RG000106.
Ge, M., G. Gendt, M. Rothacher, C. Shi, and J. Liu (2008), Resolution of GPS carrier-phase ambiguities in precise point positioning (PPP) with daily observations, *J. Geod.*, *82*(7), 389–399.
Geng, J., X. Meng, A. H. Dodson, and F. N. Teferle (2010), Integer ambiguity resolution in precise point positioning: Method comparison, *J. Geod.*, *84*, 569–581.
Haase, J. S., J. Maldonado-Vargas, F. Rabier, P. Cocquerez, M. Minois, V. Guidard, P. Wyss, and A. V. Johnson (2012), A proof-of-concept balloon-borne GPS radio occultation profiling system for polar studies, *Geophys. Res. Lett.*, *39*, L02803, doi:10.1029/2011GL049982.
Hamilton, K. (1995), Comprehensive simulation of the middle atmospheric climate: Some recent results, *Clim. Dyn.*, *11*, 223–241.
Hertzog, A., and F. Vial (2001), A study of the dynamics of the equatorial lower stratosphere by use of ultra-long-duration balloons 2. Gravity waves, *J. Geophys. Res.*, *106*, 22,745–22,761, doi:10.1029/2000JD000242.
Hertzog, A., F. Vial, C. R. Mechoso, C. Basdevant, and P. Cocquerez (2002), Quasi-Lagrangian measurements in the lower stratosphere reveal an energy peak associated with near-inertial waves. *Geophys. Res. Lett.*, *29*(8), 1229, doi:10.1029/2001GL014083.
Hertzog, A., G. Boccara, R. Vincent, F. Vial, and P. Cocquerez (2008), Estimation of gravity wave momentum flux and phase speeds from quasi-Lagrangian stratospheric balloon flights. Part II: Results from the Vorcore campaign in Antarctica, *J. Atmos. Sci.*, *65*, 3056–3070.
Hertzog, A., M. J. Alexander, and R. Plougonven (2012), On the intermittency of gravity wave momentum flux in the stratosphere, *J. Atmos. Sci.*, *69*, 3433–3448.
Hindley, N. P., C. J. Wright, N. D. Smith, and N. J. Mitchell (2015), The southern stratospheric gravity wave hot spot: Individual waves and their momentum fluxes measured by COSMIC GPS-RO, *Atmos. Chem. Phys.*, *15*, 7797–7818, doi:10.5194/acp-15-7797-2015.
Hoffmann, L., X. Xue, and M. J. Alexander (2013), A global view of stratospheric gravity wave hotspots located with Atmospheric Infrared Sounder observations, *J. Geophys. Res. Atmos.*, *118*, 416–434, doi:10.1029/2012JD018658.
Höpfner, M., et al. (2006), MIPAS detects Antarctic stratospheric belt of NAT PSCs caused by mountain waves, *Atmos. Chem. Phys.*, *6*, 1221–1230.
Jewtoukoff, V., A. Hertzog, R. Plougonven, A. Cámara, and F. Lott (2015), Comparison of gravity waves in the Southern Hemisphere derived from balloon observations and the ECMWF analyses, *J. Atmos. Sci.*, *72*, 3449–3468.
John, S. R., and K. K. Kumar (2016), HIRDLS observations of global gravity wave absolute momentum fluxes: A wavelet based approach, *J. Atmos. Sol. Terr. Phys.*, *138-139*, 74–86.
Julian, P., V. E. Lally, W. Kellogg, V. Suomi, and C. Cote (1977), The TWERL experiment, *Bull. Am. Meteorol. Soc.*, *58*, 936–948.
Kim, Y.-J., S. Eckermann, and H.-Y. Chun (2003), An overview of the past, present and future of gravity-wave drag parametrization for numerical climate and weather prediction models, *Atmos. Ocean*, *41*, 65–98.
Lemoine, F. G., et al. (1998), The development of the joint NASA GSFC and NIMA geopotential model EGM96, *Rep. TM-1998-206861*, NASA, Greenbelt, Md.
Lou, Y., W. Zhang, C. Wang, X. Yao, C. Shi, and J. Liu (2014), The impact of orbital errors on the estimation of satellite clock errors and PPP, *Adv. Space Res.*, *54*(8), 1571–1580.
Plougonven, R., A. Hertzog, and H. Teitelbaum (2008), Observations and simulations of a large-amplitude mountain wave breaking above the Antarctic Peninsula, *J. Geophys. Res.*, *113*, D16113, doi:10.1029/2007JD009739.
Rabier, F., et al. (2010), The CONCORDIASI project in Antarctica, *Bull. Am. Meteorol. Soc.*, *91*, 69–86.
Saastamoinen, J. (1972), Atmospheric correction for the troposphere and stratosphere in radio ranging of satellites, in *The Use of Artificial Satellites for Geodesy*, *Geophys. Monogr. Ser.*, vol. 15, pp. 247–251, AGU, Washington, D. C.
Schmid, R., P. Steigenberger, G. Gendt, M. Ge, and M. Rothacher (2007), Generation of a consistent absolute phase-center correction model for GPS receiver and satellite antennas, *J. Geod.*, *81*(12), 781–798.
Shi, C., Q. Zhao, J. Geng, Y. Lou, M. Ge, and J. Liu (2008), Recent development of PANDA software in GNSS data processing, paper 72851S presented at International Conference on Earth Observation Data Processing and Analysis (ICEODPA), doi:10.1117/12.816261.
Torrence, C., and G. P. Compo (1998), A practical guide to wavelet analysis, *Bull. Am. Meteorol. Soc.*, *79*, 61–78.
Tsuda, T., M. Nishida, C. Rocken, and R. H. Ware (2000), A global morphology of gravity wave activity in the stratosphere revealed by GPS occultation data (GPS/MET), *J. Geophys. Res.*, *105*, 7257–7273, doi:10.1029/1999JD901005.

Vial, F., A. Hertzog, C. R. Mechoso, C. Basdevant, P. Cocquerez, V. Dubourg, and F. Nouel (2001), A study of the dynamics of the equatorial lower stratosphere by use of ultra-long-duration balloons, 1. Planetary scales, *J. Geophys. Res.*, *106*, 22,725–22,743, doi:10.1029/2000JD000241.

Vincent, R. A., and A. Hertzog (2014), The response of superpressure balloons to gravity wave motions, *Atmos. Meas. Tech.*, *7*, 1043–1055, doi:10.5194/amt-7-1043-2014.

Vincent, R. A., and I. M. Reid (1983), HF Doppler measurements of mesospheric gravity wave momentum fluxes, *J. Atmos. Sci.*, *40*, 1321–1333.

Vincent, R. A., A. Hertzog, G. Boccara, and F. Vial (2007), Quasi-Lagrangian superpressure balloon measurements of gravity wave momentum fluxes in the polar stratosphere of both hemispheres, *Geophys. Res. Lett.*, *34*, L19804, doi:10.1029/2007GL031072.

Watanabe, S., Y. Kawatani, Y. Tomikawa, K. Miyazaki, M. Takahashi, and K. Sato (2008), General aspects of a T213L256 middle atmosphere general circulation model, *J. Geophys. Res.*, *113*, D12110, doi:10.1029/2008JD010026.

Welch, P. D. (1967), The use of fast fourier transform for the estimation of power spectra: A method based on time averaging over short, modified periodograms, *IEEE Trans. Audio Electroacoust.*, *15*, 70–73.

Wright, C. J., S. M. Osprey, and J. C. Gille (2013), Global observations of gravity wave intermittency and its impact on the observed momentum flux morphology, *J. Geophys. Res. Atmos.*, *118*, 10,980–10,993, doi:10.1002/jgrd.50869.

Wright, C. J., S. M. Osprey, and J. C. Gille (2015), Global distributions of overlapping gravity waves in HIRDLS data, *Atmos. Chem. Phys.*, *15*, 8459–8477, doi:10.5194/acp-15-8459-2015.

Wu, J., S. Wu, G. Hajj, W. Bertiger, and S. Lichten (1993), Effect of antenna orientation on GPS carrier phase, *Manuscr. Geod.*, *18*, 91–98.

Wu, D. L., and J. H. Jiang (2002), MLS observations of atmospheric gravity waves over Antarctica, *J. Geophys. Res.*, *107*(D24), 4773, doi:10.1029/2002JD002390.

Zumberge, J., M. Heflin, D. Jefferson, M. Watkins, and F. Webb (1997), Precise point positioning for the efficient and robust analysis of GPS data from large networks, *J. Geophys. Res.*, *102*, 5005–5017, doi:10.1029/96JB03860.